

Small-Animal PET Imaging of Tau Pathology with ^{18}F -THK5117 in 2 Transgenic Mouse Models

Matthias Brendel^{1*}, Anna Jaworska^{2*}, Federico Probst¹, Felix Overhoff¹, Viktoria Korzhova², Simon Lindner¹, Janette Carlsen¹, Peter Bartenstein^{1,3}, Ryuichi Harada⁴, Yukitsuka Kudo⁴, Christian Haass^{2,3,5}, Fred Van Leuven⁶, Nobuyuki Okamura⁴, Jochen Herms^{2,3}, and Axel Rominger^{1,3}

¹Department of Nuclear Medicine, Ludwig-Maximilians-University of Munich, Munich, Germany; ²German Center for

Neurodegenerative Diseases (DZNE), Munich, Germany; ³Munich Cluster for Systems Neurology (SyNergy), Munich, Germany;

⁴Tohoku University, Sendai, Japan; ⁵Biomedical Center (BMC), Ludwig-Maximilians-University of Munich, Munich, Germany; and

⁶Experimental Genetics Group LEGTEGG, KU-Leuven, Belgium

Abnormal accumulation of tau aggregates in the brain is one of the hallmarks of Alzheimer disease neuropathology. We visualized tau deposition in vivo with the previously developed 2-arylquinoline derivative ^{18}F -THK5117 using small-animal PET in conjunction with autoradiography and immunohistochemistry gold standard assessment in 2 transgenic mouse models expressing hyperphosphorylated tau. Small-animal PET recordings were obtained in groups of P301S ($n = 11$) and biGT mice ($n = 16$) of different ages, with age-matched wild-type (WT) serving as controls. After intravenous administration of 16 ± 2 MBq of ^{18}F -THK5117, a dynamic 90-min emission recording was initiated for P301S mice and during 20–50 min after injection for biGT mice, followed by a 15-min transmission scan. After coregistration to the MRI atlas and scaling to the cerebellum, we performed volume-of-interest-based analysis (SUV ratio [SUVR]) and statistical parametric mapping. Small-animal PET results were compared with autoradiography ex vivo and in vitro and further validated with AT8 staining for neurofibrillary tangles. SUVRs calculated from static recordings during the interval of 20–50 min after tracer injection correlated highly with estimates of binding potential based on the entire dynamic emission recordings ($R = 0.85$). SUVR increases were detected in the brain stem of aged P301S mice ($+11\%$; $P < 0.001$) and in entorhinal/amygdaloid areas ($+15\%$; $P < 0.001$) of biGT mice when compared with WT, whereas aged WT mice did not show increased tracer uptake. Immunohistochemical tau loads correlated with small-animal PET SUVR for both P301S ($R = 0.8$; $P < 0.001$) and biGT ($R = 0.7$; $P < 0.001$) mice, and distribution patterns of AT8-positive neurons matched voxelwise statistical parametric mapping analysis. Saturable binding of the tracer was verified by autoradiographic blocking studies. In the first dedicated small-animal PET study in 2 different transgenic tauopathy mouse models using the tau tracer ^{18}F -THK5117, the temporal and spatial progression could be visualized in good correlation with gold standard assessments of tau accumulation. The serial small-animal PET method could afford the means for preclinical testing of novel therapeutic approaches by accommodating interanimal variability at baseline, while detection thresholds in young animals have to be considered.

Key Words: Alzheimer's disease; tauopathy; small animal PET; transgenic mice; ^{18}F -THK5117

J Nucl Med 2016; 57:792–798

DOI: 10.2967/jnumed.115.163493

Alzheimer disease (AD) is the most frequent cause of dementia, with an exponentially increasing incidence as a function of age among the elderly. This epidemic is imposing an increasingly onerous burden on health care in societies with aging populations (1). There is an urgent need to find new biomarkers predictive of clinical course and also serving as outcome measures in clinical trials of innovative disease-modifying agents (2). The main neuropathologic features of AD, which include the accumulation of extracellular β -amyloid plaques and intracellular neurofibrillary tangles (3), are emulated in transgenic (TG) animal models (4–6). Small-animal PET has emerged as a useful tool for translational research involving longitudinal in vivo imaging of β -amyloid and tau pathology in rodent models (7,8).

Although β -amyloid small-animal PET in TG mice has been successfully established for preclinical in vivo imaging (9–11), there have been few reports on tau small-animal PET data in wild-type (WT) and TG mice (12,13). Successful molecular imaging with ^{18}F -fluorinated radiotracers of neurofibrillary tangle accumulation is a recent development (14); the 2-arylquinoline derivative ^{18}F -THK5117 has shown high affinity for neurofibrillary tangles in vitro and in brain sections from AD patients (13). However, the suitability of this agent for monitoring the accumulation of neurofibrillary tangles by small-animal PET in mice with tau pathology remains to be established.

The aim of this small-animal PET study was therefore to investigate the sensitivity of small-animal PET with the tracer ^{18}F -THK5117 in 2 TG mouse models with tau overexpression and to compare several approaches for small-animal PET quantitation, validated relative to immunohistochemistry, and additionally by autoradiography in vitro.

MATERIALS AND METHODS

Radiochemistry

Radiosynthesis of ^{18}F -THK5117 was performed as previously described (15) with slight modifications detailed in the supplemental

Received Jul. 13, 2015; revision accepted Jan. 21, 2016.

For correspondence or reprints contact: Axel Rominger, University of Munich, Marchioninistrasse 15, 81377 Munich, Germany.

E-mail: axel.rominger@med.uni-muenchen.de

*Contributed equally to this work.

Published online Feb. 11, 2016.

COPYRIGHT © 2016 by the Society of Nuclear Medicine and Molecular Imaging, Inc.

materials (available at <http://jnm.snmjournals.org>), yielding a radiochemical purity of greater than 98% and specific activity of 202 ± 56 GBq/ μ mol at the end of synthesis.

Animals

All experiments were performed in compliance with the National Guidelines for Animal Protection (Germany) and approval of the animal care committee (Regierung Oberbayern), with supervision by a veterinarian. Two TG mouse models were investigated in this study: Tau-P301S mice (P301S) and bigenic GSK-3 β \times Tau-P301L (biGT) mice, together with age-matched WT controls. Details on the animal models are provided in the supplemental materials.

Tau Small-Animal PET

Study Overview. A detailed overview of the different groups of mice and investigations performed is presented in Table 1. Test–retest small-animal PET scans were acquired in a subset of 7 P301S and C57BL/6 animals within 1 wk, using identical scanning parameters. To investigate the optimal time window for small-animal PET quantitation, complete 90-min dynamic recordings were acquired in P301S and corresponding WT mice; findings from these pilot scans defined the optimal acquisition window to be used in the larger biGT cohort.

Data Acquisition and Analyses. Data acquisition and reconstruction information is provided in the supplemental materials. In brief, summed dynamic (0–90 min after injection for P301S) and static frames (20–50 min after injection for biGT) were coregistered to an MRI mouse atlas (16) by a manual rigid-body transformation using the PMOD fusion tool (V3.5; PMOD Technologies Ltd.). The interpreter was masked to the type of mouse. A second experienced interpreter ensured accurate alignment. Volumes of interest (VOIs) were defined on the MRI mouse atlas (Fig. 1). In P301S animals receiving the full dynamic small-animal PET scan, parametric maps of binding potential (BP_{ND}) were calculated using a linear graphic method (17), with the cerebellar VOI serving as pathology-free reference tissue. Time–activity–curves of the brain stem, cranium, Harderian glands, and whole brain were extracted. Reference and target VOIs were used for calculation of 18 F-THK5117 brain stem–to–cerebellum ($SUV_{R_{BST/CBL}}$ in P301S) and entorhinal/amygdaloid–to–cerebellum SUV ratios ($SUV_{R_{ENT/CBL}}$ in biGT) of the 20- to 50-min frame.

Interpreter-Independent Coregistration. For final VOI- and statistical parametric mapping (SPM)–based small-animal PET analyses, an interpreter-independent coregistration was established after validation of the optimal 20- to 50-min window. Further details are provided in the supplemental materials.

SPM. For whole-brain voxelwise comparisons between groups of TG versus pooled WT mice, SPM was performed using SPM5 routines (Wellcome Department of Cognitive Neurology) implemented in MATLAB (version 7.1; MathWorks Inc.) (10). Individual SUV maps from TG mice were also compared with pooled WT mice to calculate for each mouse a voxelwise z score map expressing the divergence in SDs from the WT group. Furthermore, we performed linear regression with tau load (%) as a vector in the entire groups of (young and old) P301S and biGT mice.

Immunohistochemistry

After completion of the final small-animal PET scans, phosphorylated tau was detected in postfixed brains with the monoclonal AT8 antibody (Thermo Scientific), which recognizes phospho-paired helical filaments-tau, phosphorylated at Ser202 and Thr205. A more detailed description of immunohistochemistry is provided in the supplemental materials. Tau load (%) was calculated as the summed area of all tau-positive cells relative to the area of regions of interest. These analyses were performed by an operator masked to the small-animal PET results.

Ex Vivo and In Vitro Autoradiography

Ex vivo autoradiography was performed in a subset of P301S and C57BL/6 animals killed while deeply anesthetized at 50 min after injection of 15.2 ± 3.4 MBq of 18 F-THK5117, administered in 150 μ L of saline to a tail vein. In vitro autoradiography was performed in these and further mice; an overview of methods is shown in Table 1. A detailed description of the procedure is provided in the supplemental materials.

Statistics

Group comparisons of VOI-based small-animal PET results between TG cohorts and WT mice were assessed by 1-way ANOVA and the Tukey post hoc test for multiple comparisons using IBM SPSS Statistics (version 22.0; SPSS). For correlation analyses, Pearson coefficients of correlation (R) were calculated. A threshold of P less than 0.05 was considered to be significant for rejection of the null hypothesis. For the voxelwise group comparison of TG versus WT mice, 2-sample t tests were performed, with a significance threshold of P less than 0.001, uncorrected for multiple comparisons.

RESULTS

Dynamic VOI-Based Analyses and Methodology

VOI-based analyses of the dynamic small-animal PET data from P301S and C57BL/6 mice were performed to investigate 18 F-THK5117 kinetics in the brain in relation to the influence of

TABLE 1
Study Overview

Mouse strain	Age (mo)	Mean weight \pm SD (g)	Small-animal PET scan (n)	Immunohistochemistry AT8 staining (n)	Autoradiography ex vivo (n)	Autoradiography in vitro (n)	Mean small-animal PET SUVR \pm SD for brain stem	Mean AT8 tau load \pm SD (%)	Mean small-animal PET SUVR \pm SD for entorhinal/amygdala	Mean AT8 tau load \pm SD (%)
P301S	5.5	28.3 \pm 4.1	4	2	2	2	1.15 \pm 0.04	10.4/11.2		
	8–11	26.1 \pm 5.8	7	7	3	3	1.31 \pm 0.05*	38.6 \pm 20.0		
WT	6–22	30.4 \pm 4.8	25	2	5	5	1.17 \pm 0.05	0		
biGT	12	29.7 \pm 4.5	8	8		2			1.16 \pm 0.04*	11.4 \pm 7.4
	21	28.1 \pm 5.5	8	8		2			1.17 \pm 0.03*	14.3 \pm 5.8
WT	6–22	30.4 \pm 4.8	25	2	5	5			1.01 \pm 0.04	0

* $P < 0.001$; 2-sample t test.

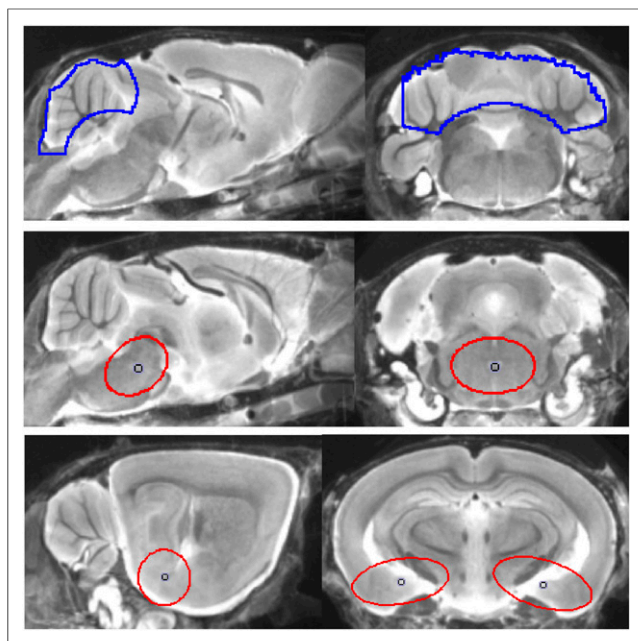


FIGURE 1. Definitions of VOIs projected on mouse brain MRI atlas (16) in sagittal and coronal slices: cerebellar VOI (top row; 55 mm³; blue line), oval-shaped brain stem VOI including central parts of pons and mid-brain (middle row; 11 mm³; red line), and bilateral spheric entorhinal cortex/amygdala (bottom row; 7 mm³ each; red line).

spillover from extracerebral structures and to define an optimal time window for static small-animal PET recordings. Mean (\pm SD) brain stem-to-cerebellum ratios in P301S mice aged 5.5 and 8–11 mo and for pooled WT mice aged 6–12 mo are shown in Figure 2A. Extracerebral activities (cranium, Harderian glands) in relation to whole-brain activity are shown in Figure 2B. The time-activity curves suggest the attainment of equilibrium binding in the brain by about 15 min after injection. Cranial uptake exceeded brain activity at times after 25 min, and progressive uptake in Harderian glands gives rise to potential cerebral spill-in after 50 min. These findings together suggested the use of an early static time frame to avoid distortion of brain time-activity curves. Additionally, attention was required for assessing ¹⁸F-THK5117 uptake in the frontal brain because this region was potentially vulnerable to spill-in from the Harderian glands, even at early time points.

There was a high correlation of BP_{ND} in all VOIs calculated for the entire 90-min recordings with the SUVR ($R = 0.85$, $P < 0.001$) for the time frame 20–50 min after injection (Fig. 2C). Test-retest analyses showed 20- to 50-min $SUVR_{BST/CBL}$ values in the entire study group to be robust for the brain stem target region ($R = 0.95$, $P < 0.001$; Fig. 2D). The mean variability in test-retest in that VOI was 1.2%, with a maximum variability of 2.5%.

VOI-Based Small-Animal PET Analyses

VOI-based analyses revealed significant SUVR differences in the brain stem of aged P301S animals compared with pooled WT mice (+11%; $P < 0.001$) (Fig. 3A; Table 1). In the younger P301S mice examined at the age of 5.5 mo, the brain stem signal was in the range of WT mice (1.18 ± 0.04 vs. 1.16 ± 0.05). There was a significantly higher ¹⁸F-THK5117 uptake in the entorhinal

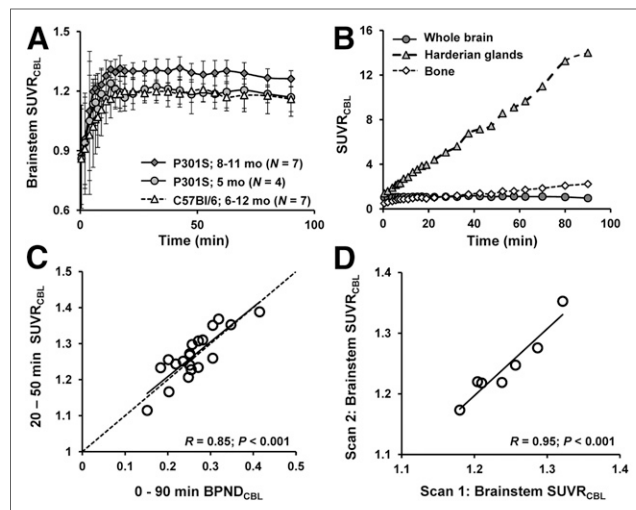


FIGURE 2. (A) Brain stem-to-cerebellum ratios as functions of time after ¹⁸F-THK5117 administration in groups of 5.5- and 8- to 11-mo-old TG P301S mice and pooled C57BL/6 WT mice (6–12 mo). Error bars are SD. (B) Tissue-to-cerebellum ratios as functions of time after ¹⁸F-THK5117 administration as assessed in 4 mice with C57BL/6 background demonstrating substantial cranial uptake. (C) Correlation of ¹⁸F-THK5117 BP_{ND} assessed from 90-min dynamic small-animal PET recordings with SUVR results (brain stem/cerebellum) from 20- to 50-min static frame, estimated from brain stem VOI in all TG and WT mice. Dotted line is line of identity ($BP_{ND} = SUVR-1$). (D) Test-retest correlation of brain stem-to-cerebellum SUVR in static 20- to 50-min frame.

cortex/amygdala VOI from biGT mice at age 12 (+14.9%; $P < 0.001$) and 21 mo (+15.2%; $P < 0.001$) compared with pooled WT mice (Fig. 3B; Table 1).

Voxelwise Analyses

Voxelwise group contrasts between TG and WT animals are shown in Figure 4. From this exploratory approach, we could discern significant differences in ¹⁸F-THK5117 uptake between P301S and pooled WT mice in a brain stem cluster (3,105 voxels; $P < 0.01$). The largest uptake differences in biGT versus pooled WT SUVR were found in a cluster comprising the entorhinal and piriform cortices as well as in the amygdalo-hippocampal formation and the lateral hypothalamus at age 12 (109,366 voxels; $P < 0.001$) and 21 (138,786 voxels; $P < 0.001$) mo. Smaller clusters for both biGT groups were also observed in the parietal and frontal neocortex (12 mo, 6,204 voxels, $P < 0.001$; 21 mo, 6,605 voxels, $P < 0.001$), whereas an additional cluster spreading along the piriform and orbitofrontal cortices and into the basal forebrain (17,630 voxels; $P < 0.001$) was distinctly apparent in aged biGT mice.

Immunohistochemical Validation

P301S mice revealed AT8-positive tau deposition predominantly in the brain stem, and penetrating into the cerebellar peduncles, lesser amounts in the forebrain, and complete absence in the cerebellar hemispheres. In the 2 mice examined at the age of 5.5 mo, the brain stem tau loads were 10% and 11%, whereas in 8- to 11-mo-old P301S mice, the mean brain stem tau load was $39\% \pm 20\%$ ($n = 7$; range, 15%–65%). Small-animal PET results correlated highly with the immunohistochemical quantitation of tau deposits in the brain stem ($R = 0.8$; $P < 0.001$; Fig. 5A). A cluster of significant correlation was found in the central part of

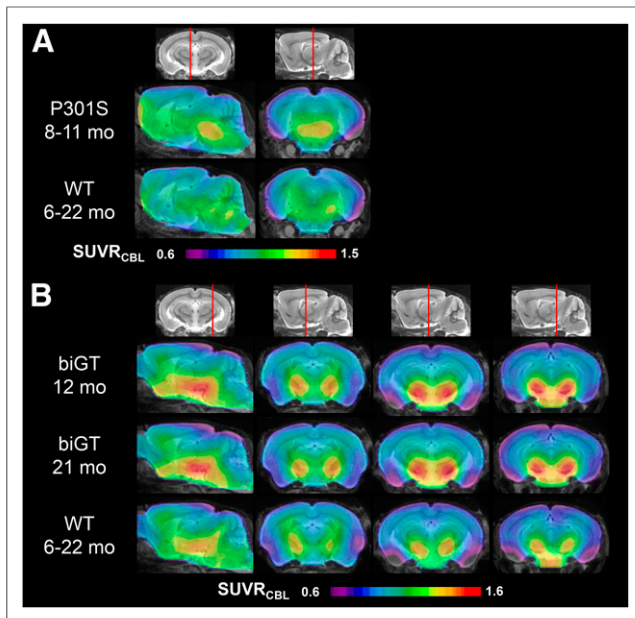


FIGURE 3. Mean parametric SUVR images in sagittal and coronal planes of ^{18}F -THK5117 uptake for aged P301S and WT controls (A) and likewise for young and old biGT and WT controls (B) projected on MRI mouse atlas (gray scale).

the brain stem (4,078 voxels; $P < 0.05$; Fig. 5A), whereas the patterns of z score maps deriving from single-mouse SPM were consistently congruent with the pattern of AT8 staining (Fig. 5A).

biGT mice showed a distinct regional distribution of AT8-positive tau deposits, with highest amounts in the entorhinal/hippocampal formation, and with lesser amounts in the basal forebrain. One of 8 mice aged 12 mo was tau-negative, with a mean entorhinal/amygdala tau load of $11.4\% \pm 7.4\%$ (range, 0.0%–19.4%). All biGT mice aged 21 mo had tau deposits, with

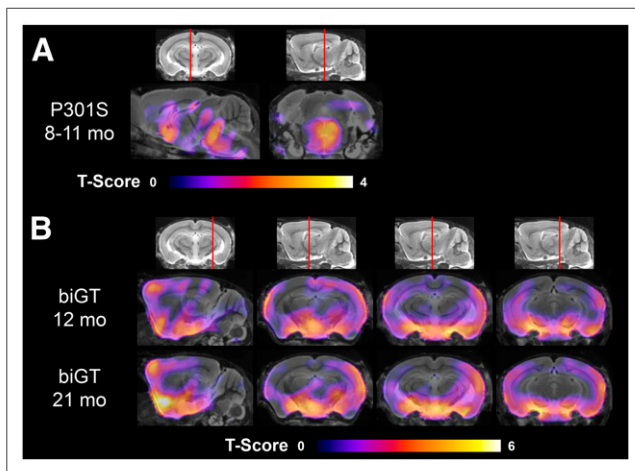


FIGURE 4. Mean voxelwise z score maps in sagittal and coronal planes of ^{18}F -THK5117 binding for groups of aged P301S vs. pooled WT mice (A) and likewise for young and old biGT mice vs. pooled WT mice (B). Results of 2-sample t test are expressed as z score maps projected on MRI mouse atlas (gray scale).

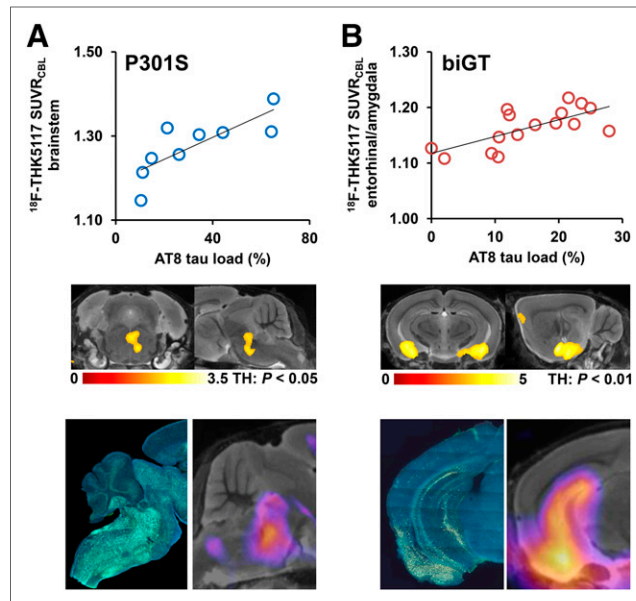


FIGURE 5. Validation of ^{18}F -THK5117 small-animal PET results by immunohistochemical AT8 staining in vitro for P301S (A) and biGT (B) mice. Top row shows correlation plots of tau load (%) in corresponding AT8-stained areas with ^{18}F -THK5117 SUVR. Middle row depicts linear regression by SPM (uncorrected for multiple comparisons, $k > 20$ voxels) between tau load (%) and small-animal PET SUVR images projected on MRI mouse atlas. Bottom row illustrates AT8-stained sections from single mice along with their individual SPM-derived z score maps (projected on MRI mouse atlas).

a group mean tau load in the inferior temporal region of $14.3\% \pm 5.8\%$ (range, 8.5%–23.8%; not significant vs. TG 12 mo). Small-animal PET results correlated highly with the immunohistochemical findings in the entorhinal/amygdala VOI ($R = 0.7$; $P < 0.001$; Fig. 5B). The 2 measures correlated significantly in bilateral clusters centered on the amygdala (49,788 voxels; $P < 0.01$; Fig. 5B), whereas the z score maps from single-mouse SPM were also congruent with the AT8 staining pattern (Fig. 5B).

Autoradiography and Blocking Experiments

Representative autoradiographic findings ex vivo and in vitro in P301S and C57BL/6 animals are illustrated along with corresponding small-animal PET binding ratio images in Figures 6A and 6B. In biGT mice, complete blocking of saturable radioligand binding was achieved by the addition of cold radioligand (Fig. 6C).

DISCUSSION

We present the first, to our knowledge, small-animal PET study with an ^{18}F -labeled radiotracer for hyperphosphorylated tau in large groups of 2 distinct TG mouse models and in WT littermates. Small-animal PET imaging with ^{18}F -THK5117 affords sensitive discrimination of tau pathology between both TG strains and WT animals, despite the several challenges presented by limited spatial resolution relative to the scale of target structures, low specific signal, and the inherent interanimal variability of tau deposition. Indeed, considerable stability of our small-animal PET procedure for in vivo quantitation of hyperphosphorylated tau burden was proven in test–retest studies, and small-animal PET gave results concurring closely with immunohistochemical findings and autoradiography. The detection of tauopathy, which is generally hampered

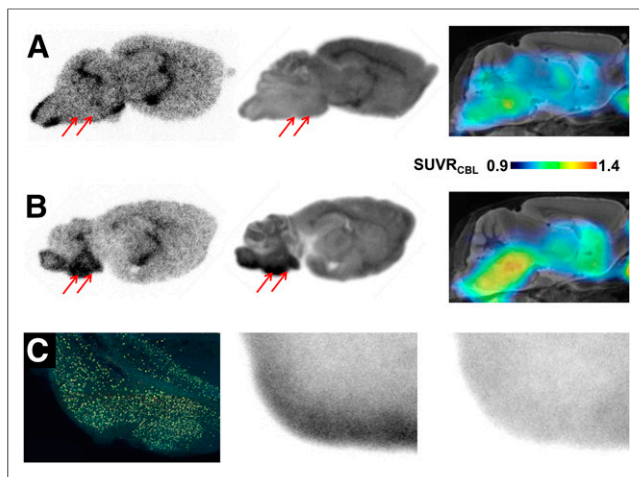


FIGURE 6. (A) Corresponding sagittal planes for autoradiography ex vivo (50 min after injection), autoradiography in vitro, and small-animal PET (SUVR_{CBL} 20–50 min after injection) from individual 12-mo-old C57BL/6 mouse expressing low ¹⁸F-THK5117 uptake in brain stem (red arrows). (B) Corresponding sagittal planes for autoradiography ex vivo (50 min after injection), autoradiography in vitro, and small-animal PET (SUVR_{CBL}; 20–50 min after injection) from 11-mo-old P301S mouse characterized by elevated ¹⁸F-THK5117 uptake in brain stem (red arrows). (C) AT8 staining in tau-rich entorhinal, postpiriform, and amygdaloid cortex of biGT mouse aged 21 mo (coronal plane), along with corresponding in vitro autoradiography of ¹⁸F-THK5117 binding without (middle) and with blocking (right) by excess nonradioactive THK5117.

by high unspecific background binding of the tracer, was enhanced by voxelwise SPM approaches.

Reference Region and Scan Window

The configuration of a suitable reference tissue region for the analysis of small-animal PET brain imaging of the rodent brain is critical. The reference region must be devoid of the targeted binding site or pathology and should provide robust reference values for semiquantitative analyses of the tau pathology (14). Our present immunohistochemical analysis showed some tau deposition in the cerebellar peduncles of aged P301S mice. Therefore, we were obliged to edit the cerebellum template so as to avoid this source of specific binding signal, which might otherwise have biased the estimation of BP_{ND} in VOIs (18).

Dynamic small-animal PET shows that ¹⁸F-THK5117 rapidly attains a plateau concentration in living mouse brain, whereas radioactivity continues to accumulate in certain extracerebral regions during prolonged small-animal PET scans. Radioactivity in the cranium, which reflects defluorination of the tracer, increases linearly with time, exceeding the global cerebral mean uptake at times after 30 min after injection. However, intense bone uptake was present only in 4 animals and was most prominent in foci within the frontal bone; as we have noted earlier in mouse small-animal PET with the dopamine receptor tracer ¹⁸F-desmethoxyfallypride (19), we do not expect substantial brain spill-in arising from bone for ¹⁸F-THK5117 scans lasting less than 60 min. However, the linear uptake in the Harderian glands soon becomes substantial and could well contaminate brain signal during late acquisition frames, especially for the near-by frontal cortex. This possibility was minimized through our use of early acquisition frames. In any case, we find that binding ratios attain a stable equilibrium in only 10 min. Binding

ratios from the 20- to 50-min static frame correlated well with BP_{ND} values from full dynamic recordings lasting 90 min. Thus, this early time window serves admirably as a convenient surrogate of the more physiologically defined BP_{ND} . Furthermore, with brief scans, the duration of anesthesia is minimized without compromising the sensitivity of the endpoint measure.

Background/Low Binding

Although SUVRs in target regions are significantly higher in P301S and biGT mice than in their controls, the magnitude of the ratios is low, even in regions with demonstrably high tau deposition. Two factors should be considered in this regard. First, the ¹⁸F-THK5117 background binding, especially in regions with abundant white matter (i.e., the brain stem), is relatively high and consequently hampers the detection of specific binding signal, even in those regions with high tau deposition. This limitation of ¹⁸F-THK5117 small-animal PET is made clear by comparing unspecific binding in WT mice and the increment in tau-positive animals, which seldom exceeds 20%, despite heavy tau load in target regions. Thus, for example, increments are relatively low in the high-background brain stem target region of aged P301S animals (1.17 SUVR background in WT; 11% difference in TG mice with 38% tau load). Quantitation is more favored in the low-background entorhinal cortex/amygdala target region of biGT mice (1.01 SUVR background in WT; 15% difference in TG with 14% tau load). We do note that an earlier investigation with ¹⁸F-THK523 in rTG4510 mice (20) found a 48% higher global brain uptake when compared with WT (21). We cannot fully account for this discrepancy but suppose that different methodologic approaches and strain-dependent tracer kinetics may be relevant factors.

A second factor in our relatively low target-binding ratios might be related to the imperfect concordance of ¹⁸F-THK5117 binding to the prevailing conformation of the tau deposits in frontotemporal dementia mice (22). Although the exact binding site of radiotracers to tau fibrils remains to be identified, the paired helical filaments described in postmortem AD material are more effectively targeted by 2-arylquinolines than is the tauopathy in frontotemporal dementia (23). Present data allow us to predict that the higher signal in small-animal PET relative to the lower tau deposition in biGT mice (in contrast to P301S) may be indicative of a more AD-like phosphorylation induced by GSK3- β , resulting in a fibrillar aggregation more similar to that observed in AD brain (24). Nevertheless, the saturable ¹⁸F-THK5117 binding in regions with high tau deposition in both mouse models was blocked by cold tracer. We used AT8 immunohistochemistry to confirm staining of tau aggregates (25), which showed colocalization with methoxy-X04 stained β -sheet structures (Supplemental Fig. 2). Although aged P301S mice contain mainly frontotemporal dementia-like half-twisted ribbons, they also express AD-like paired helical filaments (26). It remains a challenge to elucidate the affinities of ¹⁸F-THK5117 for the tau conformations prevailing in different TG mouse models; indeed, this should be a priority to be addressed in future studies.

Voxelwise Approach

Tau depositions in P301S and biGT mice are not restricted to foci but rather occur at multiple sites encompassing wide parts of the cerebrum, as is likewise the case for tau distribution in human AD pathology (27). Nonetheless, some differences in distribution

are evident in the present TG mouse models. Thus, VOI-based analyses of tau-rich regions in groups of TG mice are feasible but may miss individual heterogeneities in tau pathology. In this regard, voxelwise analyses present distinct advantages by interrogating tau levels in each voxel of the mouse brain, without prior assumptions of distribution patterns in individuals (Supplemental Fig. 1). Statistically defined voxel clusters of increased ^{18}F -THK5117 binding in our TG mouse groups matched the immunohistochemical patterns, validating group comparisons by these methods (Fig. 4). However, z score analyses in single mice proved fit for monitoring tauopathy in brains of individual mice (Fig. 5). Voxelwise comparisons present similar advantages for monitoring β -amyloid deposition by small-animal PET (10).

Suitability for In Vivo Therapy Monitoring

Despite the massive (60%) tau load in certain affected regions of aged P301S mice, we found an SUVR of only 11% increase by small-animal PET. As noted above, this discrepancy may be related to conformational hindrance of ligand binding in vivo. Moreover, P301S mice aged 8–11 mo are moribund and intolerant of narcosis compared with age-matched controls. Thus, P301S mice may not present a favorable model for prospectively monitoring antitau treatments by serial ^{18}F -THK5117 small-animal PET studies.

In contrast, biGT mice offer a longer life span, because their motor function is much less affected by tau pathology, and they manifestly tolerate narcosis and small-animal PET scans even at the old age of 21 mo. We observed regional variability in the tau deposition in entorhinal/amygdala and hippocampus regions (Supplemental Fig. 1) but only a slight increase in tau binding between 12 and 21 mo of age. As such, the biGT model may not be ideally suited for longitudinal intervention studies. However, as in our earlier experience with β -amyloid mice, sensitive detection of treatment effects should be enhanced by undertaking individual baseline small-animal PET recordings, so as to accommodate better the variability of the trajectories of pathology; baseline scanning can also be used to assign individual animals so as to obtain optimally matched subgroups, as proposed in our earlier work (28). The P301S and biGT models both showed a rather high detection threshold to small-animal PET, corresponding to approximately 10% or more tau load based on gold standard histopathologic examination. Although tau load is thus difficult to quantify in young animals, the robust detection by ^{18}F -THK5117 small-animal PET in older mice should afford the necessary sensitivity to support studies of interventional therapy.

Issues dealing with the frontal hot spot, translational aspects, and background of control animals can be found in the supplemental materials.

CONCLUSION

Preclinical in vivo imaging of tau pathology by mouse small-animal PET is feasible and gives results strongly correlating with immunohistopathologic and autoradiographic gold standard estimates. The logistically convenient 20–50 min after injection acquisition after intravenous ^{18}F -THK5117 injection yields robust and reproducible SUVRs and greatly minimizes the risk of cerebral spill-over from cranium and extracerebral sources. The relatively low ^{18}F -THK5117 target-to-reference ratios in the mouse brain need to be considered but can be compensated by voxelwise SPM data analysis, which improves the sensitivity for detecting

regional gradients in the tau pathology in single animals. In vivo assessment of the characteristic interanimal heterogeneity in tau accumulation may well enhance the statistical power of future interventional studies with follow-up to individual baseline levels. A matter still to be resolved is the impact of strain-specific configurations of tau deposition on small-animal PET studies with ^{18}F -THK5117.

DISCLOSURE

The costs of publication of this article were defrayed in part by the payment of page charges. Therefore, and solely to indicate this fact, this article is hereby marked “advertisement” in accordance with 18 USC section 1734. The study was financially supported by the Synergy Cluster, the Friedrich-Baur-Stiftung (73/15), and the Foundation for Polish Science within the International PhD project ‘Studies of nucleic acids and proteins—from basic to applied research,’ cofinanced from the European Union—Regional Development Fund (MPD/2009-3/2). No other potential conflict of interest relevant to this article was reported.

ACKNOWLEDGMENTS

A part of this paper originated from the doctoral thesis of Federico Probst. We thank Karin Bormann-Giglmair and Rosel Oos for excellent technical assistance. We thank the LEGTEGG (KULeuven) alumni for their technical and scientific contributions. The authors acknowledge Inglewood Biomedical Editing for professional editing of the manuscript.

REFERENCES

1. Ziegler-Graham K, Brookmeyer R, Johnson E, Arrighi HM. Worldwide variation in the doubling time of Alzheimer's disease incidence rates. *Alzheimers Dement*. 2008;4:316–323.
2. Weiner MW, Veitch DP, Aisen PS, et al. The Alzheimer's Disease Neuroimaging Initiative: a review of papers published since its inception. *Alzheimers Dement*. 2012;8:S1–S68.
3. Duyckaerts C, Delatour B, Potier MC. Classification and basic pathology of Alzheimer disease. *Acta Neuropathol (Berl)*. 2009;118:5–36.
4. Denk F, Wade-Martins R. Knock-out and transgenic mouse models of tauopathies. *Neurobiol Aging*. 2009;30:1–13.
5. Hall AM, Roberson ED. Mouse models of Alzheimer's disease. *Brain Res Bull*. 2012;88:3–12.
6. Teipel SJ, Buchert R, Thome J, Hampel H, Pahnke J. Development of Alzheimer-disease neuroimaging-biomarkers using mouse models with amyloid-precursor protein-transgene expression. *Prog Neurobiol*. 2011;95:547–556.
7. Zimmer ER, Leuzy A, Bhat V, Gauthier S, Rosa-Neto P. In vivo tracking of tau pathology using positron emission tomography (PET) molecular imaging in small animals. *Transl Neurodegener*. 2014;3:6.
8. Zimmer ER, Parent MJ, Cuello AC, Gauthier S, Rosa-Neto P. MicroPET imaging and transgenic models: a blueprint for Alzheimer's disease clinical research. *Trends Neurosci*. 2014;37:629–641.
9. Brendel M, Jaworska A, Griessinger E, et al. Cross-sectional comparison of small animal [^{18}F]-florbetaben amyloid-PET between transgenic AD mouse models. *PLoS One*. 2015;10:e0116678.
10. Rominger A, Brendel M, Burgold S, et al. Longitudinal assessment of cerebral beta-amyloid deposition in mice overexpressing Swedish mutant beta-amyloid precursor protein using ^{18}F -florbetaben PET. *J Nucl Med*. 2013;54:1127–1134.
11. Snellman A, Lopez-Picon FR, Rokka J, et al. Longitudinal amyloid imaging in mouse brain with ^{11}C -PIB: comparison of APP23, Tg2576, and APPsw-PS1dE9 mouse models of Alzheimer disease. *J Nucl Med*. 2013;54:1434–1441.
12. Maruyama M, Shimada H, Suhara T, et al. Imaging of tau pathology in a tauopathy mouse model and in Alzheimer patients compared to normal controls. *Neuron*. 2013;79:1094–1108.

13. Okamura N, Furumoto S, Harada R, et al. Novel ^{18}F -labeled arylquinoline derivatives for noninvasive imaging of tau pathology in Alzheimer disease. *J Nucl Med*. 2013;54:1420–1427.
14. Villemagne VL, Okamura N. In vivo tau imaging: obstacles and progress. *Alzheimers Dement*. 2014;10:S254–S264.
15. Tago T, Furumoto S, Okamura N, et al. Synthesis and preliminary evaluation of 2-arylhydroxyquinoline derivatives for tau imaging. *J Labelled Comp Radiopharm*. 2014;57:18–24.
16. Dorr A, Sled JG, Kabani N. Three-dimensional cerebral vasculature of the CBA mouse brain: a magnetic resonance imaging and micro computed tomography study. *Neuroimage*. 2007;35:1409–1423.
17. Logan J, Fowler JS, Volkow ND, Wang GJ, Ding YS, Alexoff DL. Distribution volume ratios without blood sampling from graphical analysis of PET data. *J Cereb Blood Flow Metab*. 1996;16:834–840.
18. Constantinescu CC, Mukherjee J. Performance evaluation of an Inveon PET preclinical scanner. *Phys Med Biol*. 2009;54:2885–2899.
19. Rominger A, Mille E, Boning G, et al. alpha2-adrenergic drugs modulate the binding of [^{18}F]fallypride to dopamine D2/3 receptors in striatum of living mouse. *Synapse*. 2010;64:654–657.
20. Santacruz K, Lewis J, Spire T, et al. Tau suppression in a neurodegenerative mouse model improves memory function. *Science*. 2005;309:476–481.
21. Fodero-Tavoletti MT, Okamura N, Furumoto S, et al. ^{18}F -THK523: a novel in vivo tau imaging ligand for Alzheimer's disease. *Brain*. 2011;134:1089–1100.
22. Shah M, Catafau AM. Molecular Imaging Insights into Neurodegeneration: Focus on Tau PET Radiotracers. *J Nucl Med*. 2014;55:871–874.
23. Fodero-Tavoletti MT, Furumoto S, Taylor L, et al. Assessing THK523 selectivity for tau deposits in Alzheimer's disease and non-Alzheimer's disease tauopathies. *Alzheimers Res Ther*. 2014;6:11.
24. Crespo-Biel N, Theunis C, Borghgraef P, et al. Phosphorylation of protein tau by GSK3beta prolongs survival of bigenic Tau.P301LxGSK3beta mice by delaying brainstem tauopathy. *Neurobiol Dis*. 2014;67:119–132.
25. Lemoine L, Saint-Aubert L, Marutle A, et al. Visualization of regional tau deposits using (3)H-THK5117 in Alzheimer brain tissue. *Acta Neuropathol Commun*. 2015;3:40.
26. Allen B, Ingram E, Takao M, et al. Abundant tau filaments and nonapoptotic neurodegeneration in transgenic mice expressing human P301S tau protein. *J Neurosci*. 2002;22:9340–9351.
27. Braak H, Braak E. Neuropathological staging of Alzheimer-related changes. *Acta Neuropathol (Berl)*. 1991;82:239–259.
28. Brendel M, Jaworska A, Herms J, et al. Amyloid-PET predicts inhibition of de novo plaque formation upon chronic gamma-secretase modulator treatment. *Mol Psychiatry*. 2015;20:1179–1187.